Elucidating Structural Disorder in Ultra-Thin Bi-Rich Bismuth Oxyhalide Photocatalysts

Marks, Melissa; Jeppesen, Henrik; Nielsen, Mads Lund Nygaard; Kong, Jintao; Ceccato, Marcel; van der Veen, Monique A.; Bøjesen, Espen Drath; Lock, Nina

DOI
10.1002/smll.202401413

Publication date
2024

Document Version
Final published version

Published in
Small

RESEARCH ARTICLE

NANO · MICRO small
www.small-journal.com

Elucidating Structural Disorder in Ultra-Thin Bi-Rich Bismuth Oxyhalide Photocatalysts

Melissa Marks, Henrik Jeppesen, Mads Lund Nygaard Nielsen, Jintao Kong, Marcel Ceccato, Monique A. van der Veen, Espen Drath Bøjesen, and Nina Lock**

Advancing the field of photocatalysis requires the elucidation of structural properties that underpin the photocatalytic properties of promising materials. The focus of the present study is layered, Bi-rich bismuth oxyhalides, which are widely studied for photocatalytic applications yet poorly structurally understood, due to high levels of disorder, nano-sized domains, and the large number of structurally similar compounds. By connecting insights from multiple scattering techniques, utilizing electron-, X-ray- and neutron probes, the crystal phase of the synthesized materials is allocated as layered $Bi_{24}O_{31}X_{10}$ (X = Cl, Br), albeit with significant deviation from the reported 3D crystalline model. The materials comprise anisotropic platelet-shaped crystalline domains, exhibiting significant in-plane ordering in two dimensions but disorder and an ultra-thin morphology in the layer stacking direction. Increased synthesis pH tailored larger, more ordered crystalline domains, leading to longer excited state lifetimes determined via femtosecond transient absorption spectroscopy (fs-TAS). Although this likely contributes to improved photocatalytic properties, assessed via the photooxidation of benzylamine, increasing the overall surface area facilitated the most significant improvement in photocatalytic performance. This study, therefore, enabled both phase allocation and a nuanced discussion of the structure-property relationship for complicated, ultra-thin photocatalysts.

1. Introduction

Heterogeneous photocatalysis, a technology involving the utilization of light energy in conjunction with a light-absorbing, semiconducting catalyst, shows promise for many energy, environmental, and industrial applications.[1] Photocatalysis is a multifaceted technology, encompassing concepts from catalysis, photochemistry, and crystallography. Continued advancement and future adoption of the technology are therefore dependent upon developing a nuanced understanding of the interplay of factors relating to each field, such as the reaction mechanisms and surface characteristics, the dynamics of the charges (electrons and holes) generated upon light absorption, and the structural characteristics of the catalytic material.

Bismuth oxyhalides ($Bi_aO_bX_c$, X = F, Cl, Br, I) are one class of photocatalytic materials that are increasingly studied for photocatalytic applications, including pollutant degradation,[2] organic transformations,[3] CO_2 reduction,[4] H_2 evolution via water splitting[5] and N_2 fixation.[6] Several crystallographic $Bi_aO_bX_c$ phases have been reported. All of those found in the Inorganic Crystal Structure Database (ICSD) containing the more common Cl or Br as halides are visualized in **Figure 1a**. A defining feature of most $Bi_aO_bX_c$ compounds is their layered structure, featuring covalently bound 2D Bi–O slabs sandwiched between halide layers and stacked and bound along the third dimension via weaker interactions. The range

M. Marks, M. L. N. Nielsen, M. Ceccato, E. D. Bøjesen, N. Lock
Interdisciplinary Nanoscience Centre (iNANO)
Aarhus University
Gustav Wieds Vej 14, Aarhus C 8000, Denmark
E-mail: espen.bojesen@inano.au.dk; nlock@bce.au.dk

M. Marks, M. Ceccato, N. Lock
Department of Biological and Chemical Engineering
Aarhus University
Åbogade 40, Aarhus N 8200, Denmark

H. Jeppesen
Deutsches Elektronen-Synchrotron (DESY)
Notkestr. 85, 22607 Hamburg, Germany

J. Kong, M. A. van der Veen
Department of Chemical Engineering
Technische Universiteit Delft
Delft HZ 2629, The Netherlands

E. D. Bøjesen
iMAT Aarhus University Centre for Integrated Materials Research
Aarhus University
Langelandsgade 140, Aarhus C 8000, Denmark

The ORCID identification number(s) for the author(s) of this article can be found under https://doi.org/10.1002/smll.202401413

DOI: 10.1002/smll.202401413

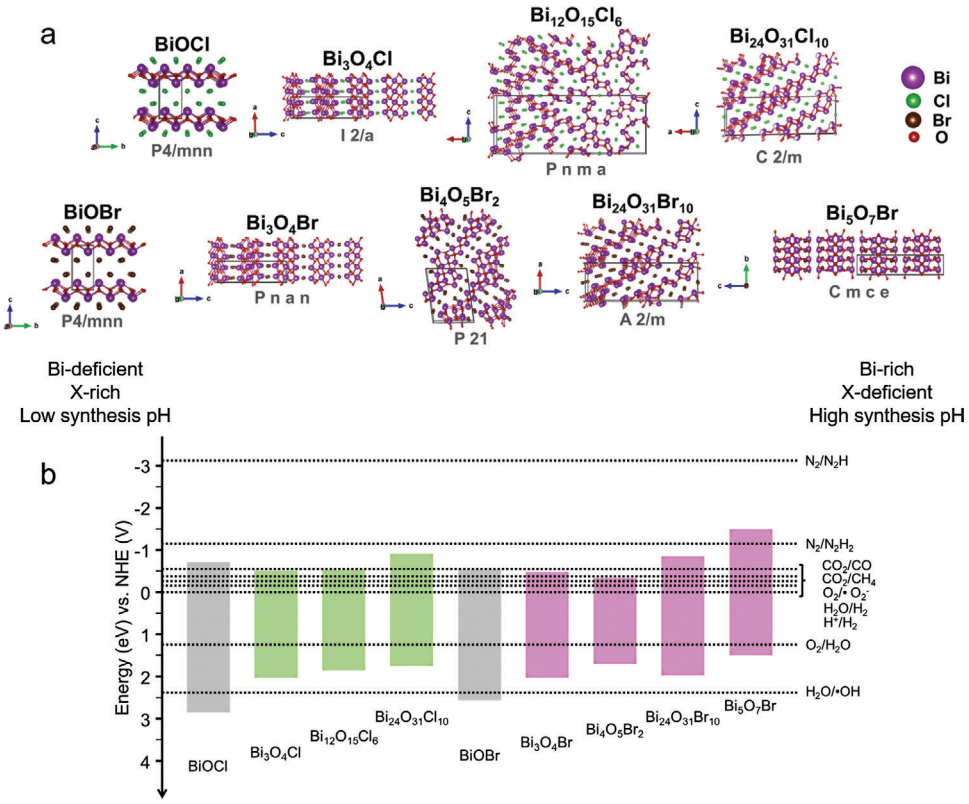

Figure 1. a) Crystal structures and database entry numbers and b) depiction of band edge positions for bismuth oxyhalide phases found in the Inorganic Crystal Structure Database, including BiOCl (#74 502),[9] Bi_3O_4Cl (#409330),[10] $Bi_{12}O_{15}Cl_6$ (#602),[11] $Bi_{24}O_{31}Cl_{10}$ (#425537),[12] BiOBr (#61225),[13] Bi_3O_4Br (#201691),[14] $Bi_4O_5Br_2$ (#412591),[15] $Bi_{24}O_{31}Br_{10}$ (#280383),[16] and Bi_5O_7Br (#241125).[17] Band edge positions were collated from several articles.[18]

of possible $Bi_aO_bX_c$ phases in Figure 1a is presented from left to right according to increasing Bi:X content ratios, and there is a consensus that "Bi-deficient" BiOX phases are formed under acidic and mildly alkaline conditions. In contrast, "Bi-rich" or "halide-deficient" phases are synthesized in strongly alkaline conditions.[7] This is thought to be facilitated by the progressive exchange of lattice halides for hydroxyls with increasing synthesis pH.[8]

Although $Bi_aO_bX_c$ materials have been studied within mineralogy and crystallography for many years,[10,19] their application as photocatalysts has only emerged in recent decades.[20] Early pioneering studies investigated the synthesis of large single crystals with preferred facet exposure for enhanced photocatalytic performance, as the anisotropic structures allow for selected facet growth under controlled synthetic conditions, most often through pH control.[5b,20a,21] Many subsequent studies have investigated alternative approaches of tailoring the materials for improved performance, including introducing surface defects and elemental deficiencies,[22] the synthesis of smaller crystallite and particle dimensions,[7c,20b] and controlling specific morphologies and nanostructures.[4b,c,23] These studies have demonstrated the tunability of phase, morphology, and properties in $Bi_aO_bX_c$ materials. A general trend is that larger surface areas (due to smaller particles) and increased concentrations of specific defects correlate with improved photocatalytic properties.[20b] However, beyond defects, the impacts of atomic-level disorder have not been elucidated.

The most Bi-deficient phases (BiOX) exhibit a comparatively simple structure, featuring small unit cells with tetragonal symmetry. The impact of synthetic conditions on the structure of these simple compounds is, therefore, widely studied and well-understood.[7c] However, an inherent drawback of BiOX materials is their wide band gap, which limits the light absorption properties by only allowing the absorption of UV light (for X = F, Cl, Br). Research efforts have therefore shifted toward the study of Bi-rich phases, which typically exhibit narrower band gaps, allowing for visible light absorption. The band edge positions of each of the $Bi_aO_bCl_c$ (green) and $Bi_aO_bBr_c$ (purple) phases found in the ICSD are visualized in Figure 1b, and the comparatively wide band gaps of BiOCl and BiOBr are highlighted in grey.

As well as improving the light absorption properties, Bi-rich phases often cause the upshifting of the conduction band (CB) potential, improving the reduction potential of the photocatalyst and therefore broadening the applicability toward sought-after photocatalytic reduction reactions, such as CO_2 reduction, H_2 evolution, and N_2 fixation.[18a,24] For example, a study by Shang et al. demonstrated the superior performance of $Bi_{24}O_{31}Br_{10}$ over BiOBr for the generation of H_2 (via H_2O splitting), attributed to the upshifting of the CB in $Bi_{24}O_{31}Br_{10}$.[25] $Bi_4O_5Br_2$ and

$Bi_{24}O_{31}Cl_{10}$ have been studied as photocatalysts for CO_2 conversion into CH_4 and CO,[26] while Bi_5O_7Br, with the most upshifted (negative) CB, has even been utilized for photocatalytic N_2 fixation.[6]

Despite the promising properties and applications of Bi-rich phases, their crystallographic nature is far less understood than their Bi-deficient BiOX counterparts. This is partially due to their greater structural complexity, as Bi-rich phases typically feature large, low-symmetry unit cells, giving rise to more complex powder X-ray diffraction (PXRD) patterns. Generally, highly crystalline forms of these Bi-rich materials are poor photocatalysts, due at least in part to the low surface areas of large crystals.[20b] The photocatalytic properties generally improve when introducing ultra-thin morphologies or defect sites,[4a,22a,24,27] further complicating the structural analysis.

A final challenge is the large number of structurally similar Bi-rich phases, which can be easily confused with each other, especially when considering highly disordered materials. Incorrect assumptions about the structure will skew subsequent discussions and conclusions about facet exposure, band structure, defect sites, or elemental deficiencies. Finally, it is widely accepted that synthetic factors such as pH and temperature can greatly impact various properties of layered bismuth oxyhalides, even when the crystal phase is unchanged.[7c,28] While the effects of these experimental factors have been studied for BiOX phases,[7a,23b] very few studies address the influence of synthesis conditions on materials synthesized at high pH, apart from the general acceptance that synthesis at high pH produces Bi-rich, halogen deficient phases.

Studies focused on elucidating the crystal phase and disordered structural characteristics of Bi-rich compounds are currently lacking. Consequently, we present a detailed structural exploration of ultra-thin and highly disordered Bi-rich $Bi_aO_bX_c$ materials. The detailed structural studies enable us to consider the connections between synthesis conditions and photophysical properties, charge carrier dynamics, and photocatalytic performance via structural characteristics. A series of Bi-rich compounds were synthesized using a microwave-assisted synthesis protocol, with systematic variations in synthesis pH facilitating the tailoring of structural characteristics. Combined synchrotron PXRD, four-dimensional scanning transmission electron microscopy (4D-STEM), and X-ray- and neutron pair distribution function (PDF) analyses were employed to elucidate these structural characteristics. The overall morphology of the synthesized materials was then considered, incorporating discussions of facet exposure, surface characteristics, and evidence for elemental deficiencies. Femtosecond transient absorption spectroscopy (fs-TAS) facilitated the investigation of trends in the generation and dissipation of photoexcited states among the synthesized materials. Finally, the suggested relationship between synthetic conditions, structure, photophysical properties, and photocatalytic performance was explored by considering the photooxidation of benzylamine as a model reaction. This study's broad, yet nuanced approach, which incorporates considerations spanning catalysis, photochemistry, and crystallography, enables one of the most detailed synthesis-structure-property-performance relationships of any photocatalytic material to date.

2. Results and Discussion

2.1. Elucidation of Crystal Phase and Microstructural Details of Ultra-Thin Bi-Rich $Bi_aO_bX_c$ Photocatalysts

The essential starting point in the present study was the assignment of the crystalline phase to allow the subsequent elucidation and rationalization of microstructural details. Due to the large number of similar Bi-rich crystal phases and the disordered nature of synthesized materials, crystal phase assignment based on the combination of synchrotron PXRD, and X-ray- and neutron PDF analyses proved inconclusive (Figure S1, Supporting Information). However, the combination of 4D-STEM (**Figure 2**b,d) and synchrotron PXRD analyses (**Figure 3**a,b) facilitated the allocation of the crystal phase of the crystalline materials as $Bi_{24}O_{31}Cl_{10}$ and $Bi_{24}O_{31}Br_{10}$ (crystal structure depicted in Figure 2a,c). Virtual annular dark field (vADF) STEM imaging reveals that the synthesized materials comprise agglomerations of ultra-thin crystalline nanosheets (Figure 2b,d). Position averaged scanning nanobeam electron diffraction patterns (PASEND) of single crystalline nanosheets (red boxes in Figures 2b,d) reveal that the individual sheets appear to be "single crystals", at least in two dimensions. The PASEND patterns can be indexed as being a [107] $Bi_{24}O_{31}Cl_{10}$ zone axis pattern and a $Bi_{24}O_{31}Br_{10}$ [$\bar{7}$01] zone axes pattern, respectively (directions are indicated in Figure 2a,c, and indexed patterns are given in Figure S2a,b, Supporting Information). These two zone axes are approximately orthogonal to the respective stacking directions of the materials ([201] and [10$\bar{2}$]); this indicates that the particles are ultrathin in the stacking directions. Moreover, analysis of the 4D-STEM data further suggests that the long-range order appears largely preserved in the in-plane directions of the material. The PASEND patterns from regions with multiple stacked nanosheets (purple boxes in Figure 2b,d) show that although the nanosheets demonstrate the same crystal structure and orientation (concerning their morphology), the agglomerated nanosheets do not necessarily stack together in an ordered or systematic matter in the lateral direction, i.e., orientational disorder between the different sheets in a stack exists, akin to the case of a disordered deck of cards.

The synchrotron PXRD patterns for the synthesized materials (Figure 3a,b; Figures S3 and S4, Supporting Information) show moderate resemblance to the calculated PXRD patterns for $Bi_{24}O_{31}Cl_{10}$ and $Bi_{24}O_{31}Br_{10}$. However, the high background and broadening and shifting of selected reflections complicate the interpretation of this data despite using high-resolution (HR) synchrotron radiation ($\lambda = 0.2073$ Å). The synchrotron data is compared with data recorded using a Cu-source diffractometer in Figure S4 (Supporting Information), to facilitate easier comparison with other studies. The highly anisotropic crystallite morphology is evident in the diffraction patterns by the presence of both broad and sharp reflections. The broadening of reflections results from decreased crystallite dimensions and/or increased microstrain in specific directions of the crystallites, particularly the stacking directions. Also notable is the considerable mismatch between the position and shape of the (201) and (10$\bar{2}$) reflections when comparing the experimental and calculated diffraction patterns, which indicates a disorder relating to the stacking of layers.

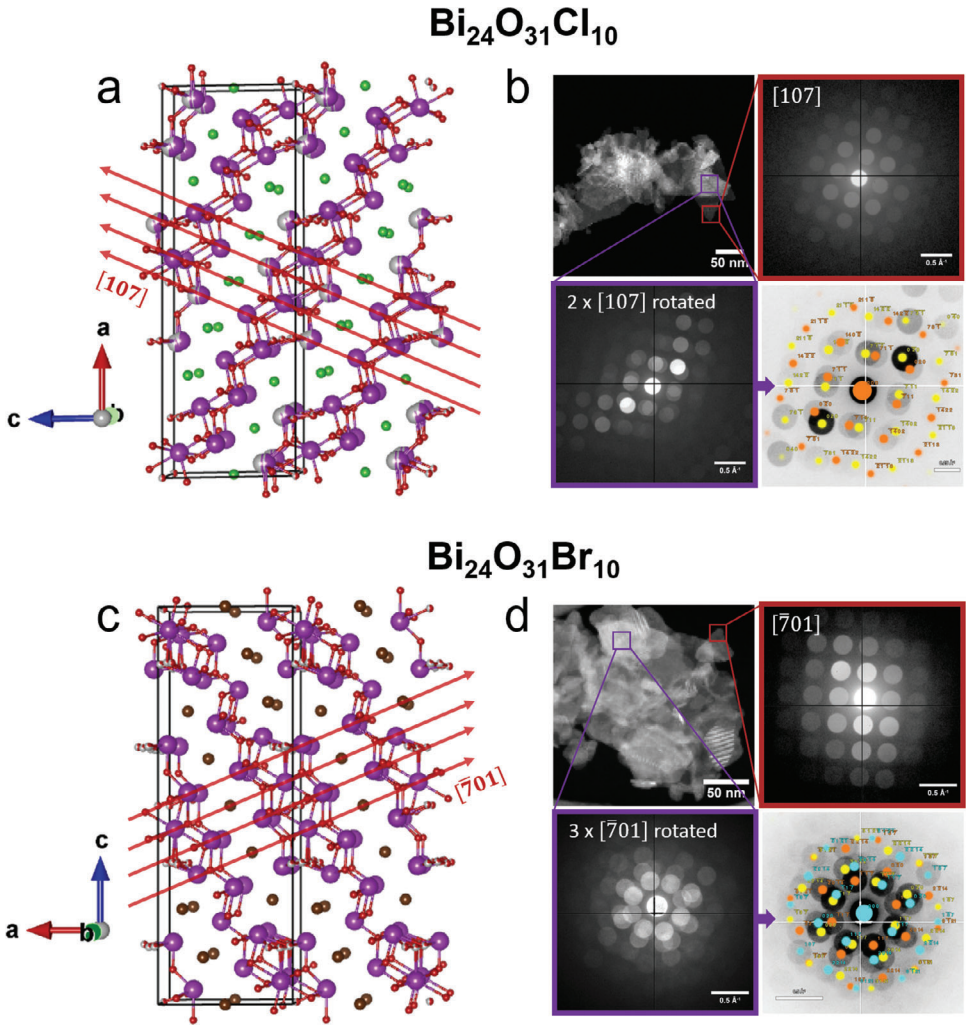

Figure 2. Crystal structures of a) $Bi_{24}O_{31}Cl_{10}$ and c) $Bi_{24}O_{31}Br_{10}$, with the [107] and [$\bar{7}$01] vectors depicted with red arrows. vADF-STEM images of b) $Bi_{24}O_{31}Cl_{10}$ and d) $Bi_{24}O_{31}Br_{10}$, with PASEND patterns from a single nanosheet (red boxes) and multiple stacked nanosheets (purple boxes), indexed as the [107] and [$\bar{7}$01] zone axis patterns, respectively. Indexed patterns for the stacked nanosheet regions are also included.

The STEM images and PASEND patterns in Figure 3c support the notion of anisotropic morphologies and high defect densities. A single well-ordered nanosheet, i.e., straight morphology when viewed edge-on, is marked in yellow in Figure 3c. This sheet has an approximate width of 7.3 nm, thus fully in line with the observed broadening of selected reflections in the PXRD patterns. The PASEND pattern from this region (yellow box, Figure 3c) is consistent with what one would expect from an edge-on view approximately orthogonal to the stacking within the crystal. The small convergence angle and accompanying broad diffraction disks rendered indexing impossible. PASEND patterns from other areas reveal that for regions with stacked nanosheets viewed edge-on (green box, Figure 3c) the PASEND patterns are much more diffuse and indicate a large degree of stacking disorder. Other regions within the sample exhibit significant disorder and strain caused by severe bending of the nanosheets, indicated with a purple box in Figure 3c.

The combined 4D-STEM and synchrotron PXRD analyses reveal that $Bi_{24}O_{31}Cl_{10}$ and $Bi_{24}O_{31}Br_{10}$ are formed under the used synthesis conditions. Furthermore, detailed structural scrutiny enables the establishment of firm connections between structure, synthesis, and microstructural properties such as anisotropy, microstrain, stacking disorder, and ultrathin regions. All these findings together inform the "historic" difficulty in proper analysis of the PXRD patterns from these materials.

2.2. The Impact of Synthesis pH on Microstructure and Atomic-Level Disorder

The close resemblance between PXRD patterns within a halide series (Figure 3a,b) indicates the equivalent crystal phase for materials synthesized within the pH range of 13.0–14.0 for $Bi_{24}O_{31}Cl_{10}$ and 12.5–14.0 for $Bi_{24}O_{31}Br_{10}$. However, small systematic variations are observed as the pH is increased. The diffraction patterns for samples synthesized at pH 12.5 or 13.0 ("lower" pH values) are akin to each other, while those for samples synthesized at pH 13.5 or 14.0 ("higher" pH values) are most

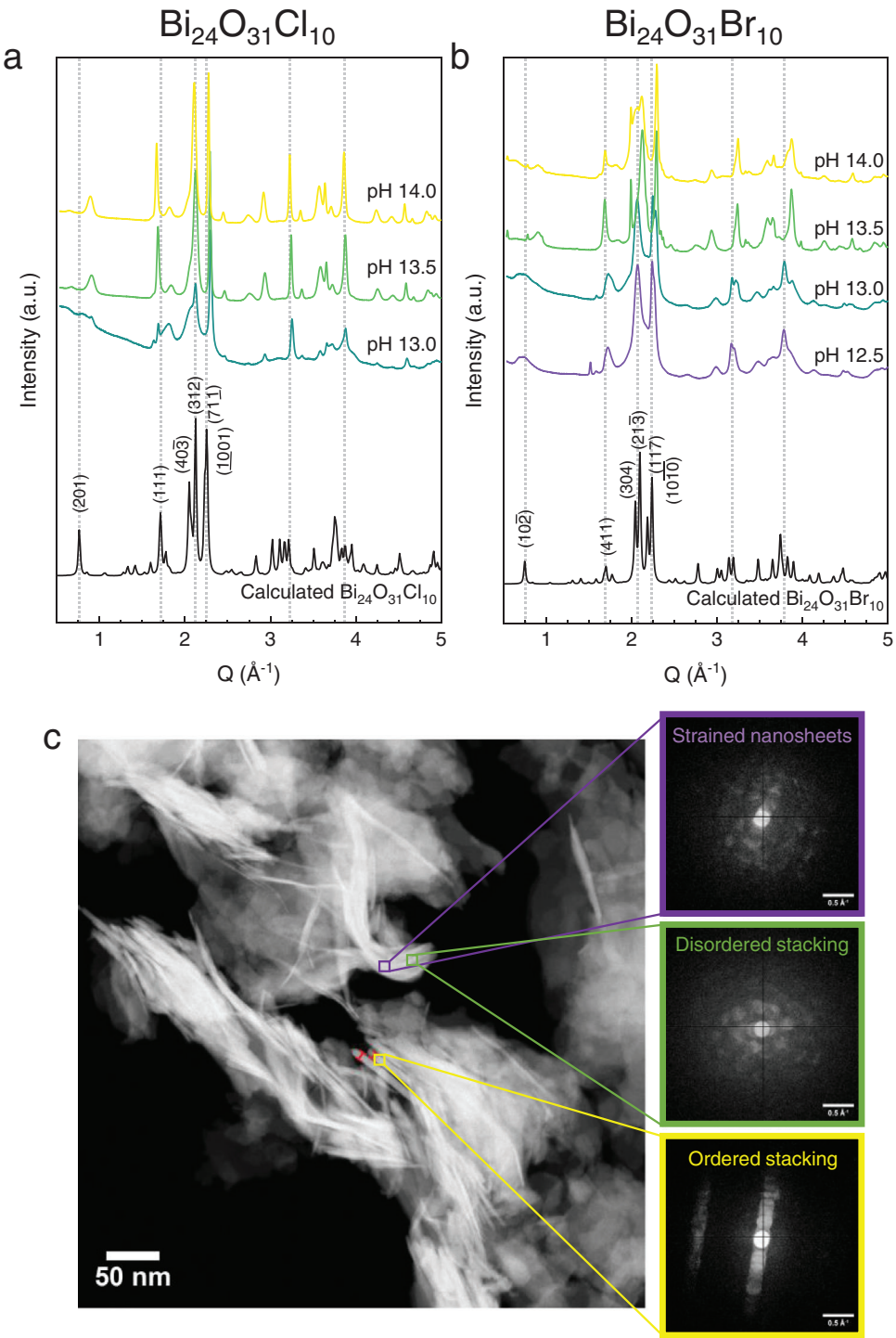

Figure 3. Synchrotron PXRD patterns for a) $Bi_{24}O_{31}Cl_{10}$ and b) $Bi_{24}O_{31}Br_{10}$ powders synthesized at varying pH values (λ = 0.2073 Å). The calculated PXRD patterns based on CIF data for $Bi_{24}O_{31}Cl_{10}$ and $Bi_{24}O_{31}Br_{10}$ are shown in black at the bottom of the plots (ICSD entries #425537[12] and #280383,[16] respectively). c) STEM image of $Bi_{24}O_{31}Cl_{10}$ synthesized at pH 13.0, with insets showing the PASEND patterns in regions with a single straight nanosheet (yellow box), multiple stacked nanosheets (green box), and multiple stacked nanosheets that exhibit significant bending (purple box).

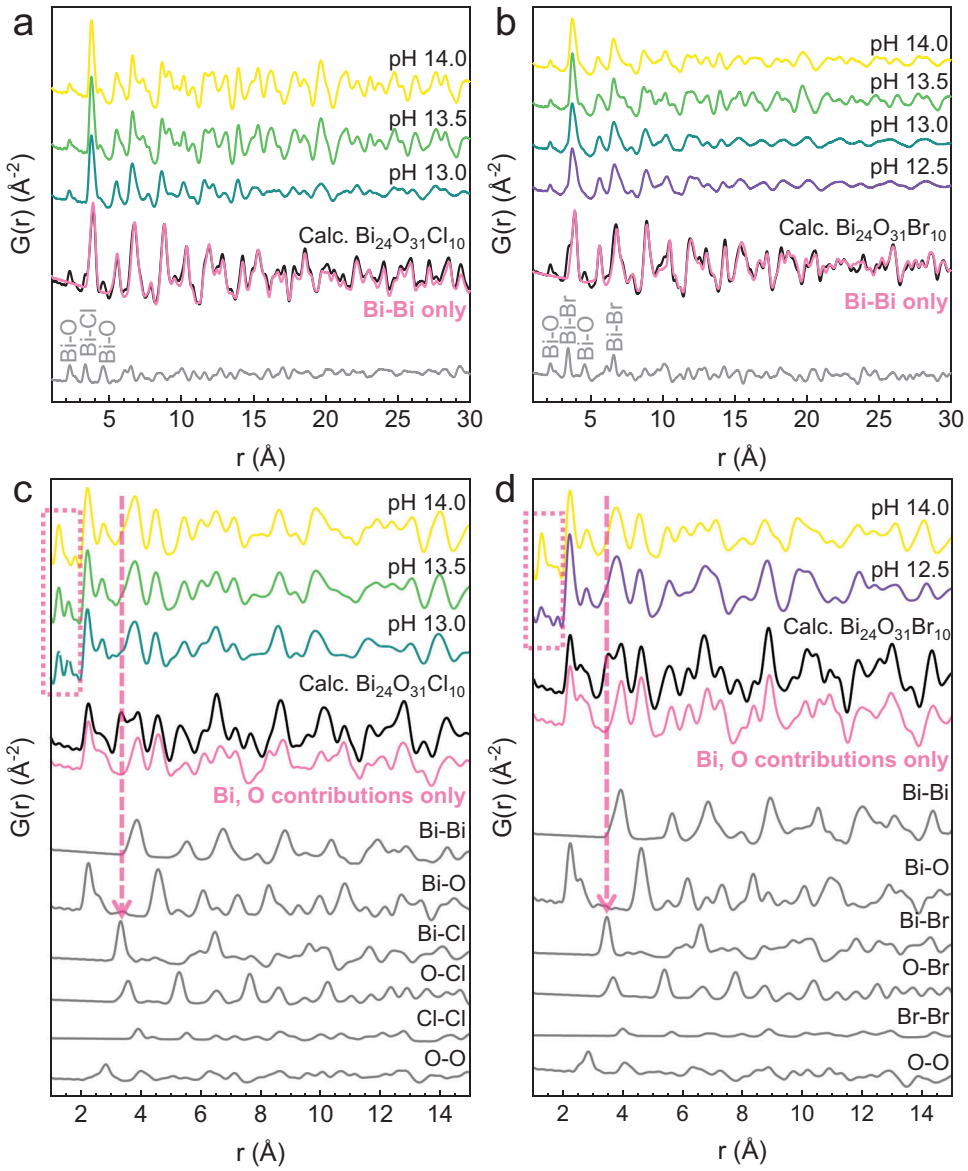

Figure 4. X-ray PDFs for a) $Bi_{24}O_{31}Cl_{10}$ and b) $Bi_{24}O_{31}Br_{10}$ samples over the r-range of 1–30 Å, compared with the calculated X-ray PDFs (black solid line), calculated Bi-Bi correlations (pink solid line), and combined contributions of all other elements (grey solid line). Neutron PDFs for c) $Bi_{24}O_{31}Cl_{10}$ and d) selected $Bi_{24}O_{31}Br_{10}$ materials, compared with the total calculated neutron PDFs (black solid line), the calculated neutron PDF without any contributions from Cl or Br (pink solid line) as well as the separated interactions of all possible atomic pairings (grey solid lines). Pink dashed arrows indicate the lack of Bi-X correlations, and pink dashed boxes indicate PDF features not described by the crystalline model.

similar. The most notable contrast between the two groups of samples is the greater broadening of Bragg reflections for the lower pH materials, suggesting smaller crystallite sizes, a greater degree of microstrain, and/or a more disordered nature. Further structural investigations focused on the atomic-level disorder using X-ray- and neutron PDF analyses (**Figure 4**) were thus undertaken to elucidate the relation between microstructure, atomic structure, and apparent disorder.

PDFs are produced by Fourier transforming total scattering (TS) data, which incorporates both Bragg diffraction and diffuse scattering, and therefore, long-range crystalline order is not a requirement for extracting structural information, given that diffuse scattering arises from amorphous-, disordered-, and nanomaterials. Combining X-ray- and neutron PDF data facilitates a more detailed analysis due to the differences in scattering cross sections/form factors for different elements from the two probes. X-ray PDFs enable greater insight into the size of crystalline regions and positioning of Bi, while neutron PDFs are more sensitive to lighter elements (O, Cl, and Br). The separation of the total calculated neutron PDFs for $Bi_{24}O_{31}Cl_{10}$ and $Bi_{24}O_{31}Br_{10}$ (black solid lines) into the contributions of correlations of all possible pairs of elements (grey solid lines) in Figure 4c,d highlights the significant contributions of all elements to the neutron PDFs, in stark contrast to the X-ray PDFs (Figure 4a,b).

Table 1. Estimated sp diameters from X-ray PDF refinements, BET-specific surface areas, atomic compositions estimated from XPS data, and estimated band gaps (E_g) from DRS for $Bi_{24}O_{31}Cl_{10}$ and $Bi_{24}O_{31}Br_{10}$ powders synthesized at varying pH.

	sp diameter [nm]	BET surface area [$m^2.g^{-1}$]	XPS atomic ratios [Bi:O:X]	E_g [eV]
$Bi_{24}O_{31}Cl_{10}$				
pH 13.0	3.5	66	24:29:3	2.5
pH 13.5	5.0	46	24:29:2	2.5
pH 14.0	4.8	36	24:28:2	2.4
$Bi_{24}O_{31}Br_{10}$				
pH 12.5	3.2	36	24:23:9	2.6
pH 13.0	3.2	43	24:26:7	2.6
pH 13.5	5.0	44	24:31:4	2.4
pH 14.0	5.1	52	24:28:4	2.5

The experimental PDFs were subjected to Pearson's correlation analysis (Tables S1, S2, Supporting Information), which reveals that all experimental PDFs within a halide series are highly similar. Yet, each PDF is most similar to the PDF synthesized at an adjacent pH interval. This is exemplified by the 99% similarity between the $Bi_{24}O_{31}Cl_{10}$ samples synthesized at pH 13.5 and 14.0, compared with only an 81% similarity between the samples synthesized at pH 13.0 and 14.0. The most striking difference distinguishing the PDFs within each halide series is the extent of dampening and broadening of correlations (Figure 4a,b; Figure S6, Supporting Information). The materials synthesized at lower pH exhibit both greater dampening and broadening, which suggests smaller crystallite dimensions and increased atomic-level disorder for these materials, respectively, which corroborates the observation of broader Bragg peaks exhibited by the lower pH samples in the PXRD patterns in Figure 3a,b.

The average spherical crystallite size was estimated by incorporating the *sp*-diameter into PDF refinements (**Table 1**; Tables S3, S4, Supporting Information), which suggests that the average diameter for materials synthesized at the lower pH is ≈3 nm. In comparison, the average diameter of materials synthesized at higher pH is ≈5 nm. Given that this parameter is intended for refining spherical instead of anisotropic crystalline domains, the absolute values may not be physically meaningful. However, the trends relating to synthesis pH and domain size are likely reliable, as they are consistent across all structural analyses. Further discussion of X-ray PDF refinements is given in the Supporting Information (Figures S7–S16 and Tables S3–S11, Supporting Information).

The high degree of anisotropy is evident from the X-ray- and neutron PDFs in Figure 4. For the X-ray PDFs in Figure 4a,b, the nearest neighbor Bi–Bi correlation arising at approx. 3.8 Å is over-pronounced relative to the calculated PDF based on the 3D crystalline model, which is based on an isotropic crystal shape. The 3.8 Å distance corresponds to Bi–Bi correlations found within the 2D in-plane Bi–O layers and corroborates that the long-range order is only present in two out of the three dimensions within the crystalline domains. The most prominent indication of anisotropic domains is found in the neutron PDFs in Figure 4c,d, via the lacking Bi–Cl or Bi–Br correlations (indicated with pink dashed arrows) relative to the total calculated PDF based on the isotropic 3D crystalline model. Calculating the neutron PDFs without including any contributions from Cl or Br provides a calculated PDF with a far greater resemblance to the experimental data (pink solid lines). Given that the materials comprise nanosheets with only a few layers bound in the stacking direction, and that the halides are stacked between Bi–O layers, far fewer Bi–X correlations are expected in the synthesized materials relative to the 3D crystalline model.

Finally, all experimental neutron PDFs also feature correlations arising at ≈1.3 and 1.6 Å, which increase in magnitude with pH, but are not described by the crystalline models for $Bi_{24}O_{31}Cl_{10}$ and $Bi_{24}O_{31}Br_{10}$ (pink dashed boxes in Figure 4c,d). These correlations likely result from small amounts of amorphous silica, remaining from either the leaching of glassware during synthesis conducted in highly alkaline conditions or a remnant of the background subtraction during the transformation of neutron TS data.

Combined, the X-ray- and neutron PDF analyses support the structural analyses of the long-range order via 4D-STEM and synchrotron PXRD whilst providing further information regarding the local structure. The X-ray PDFs particularly demonstrate the overall similarity in local atomic arrangement for all materials within a halide series whilst also indicating that larger crystalline domains and lesser atomic-level disorder are facilitated by increased pH. The neutron PDF analyses highlight the absence of Bi–X correlations, demonstrating that very few layers are bound together in the stacking direction. This provides strong evidence that the synthesized materials exhibit extensive long-range order in only two dimensions and significant disorder in the third dimension.

2.3. The Relationship between Synthesis pH, the Hierarchical Morphology, and Surface Characteristics

The combined structural analyses demonstrate that the small systematic changes in synthesis pH do not alter the crystal phase but rather influence the microstructure and level of disorder. The subsequent impacts on the overall morphology, elemental composition, and surface characteristics were thus studied in detail through scanning electron microscopy (SEM), N_2 adsorption/desorption, and X-ray photoelectron spectroscopy (XPS) analyses.

The SEM images in **Figure 5** demonstrate that the overall morphology of all synthesized materials can be described as irregular, micron-sized agglomerates, with flower or coral-like characteristics. As indicated by the STEM images in Figure 2b,d, the agglomerates comprise many ultra-thin nanosheets joined together in a seemingly random arrangement. The impact of synthesis pH is seen in the characteristics of the nanosheets. With increasing synthesis pH, both the size and definition of the facets increase, suggesting larger crystalline regions and lesser disorder, corroborating the earlier structural analyses. The distribution of elements throughout several materials was assessed with STEM-Energy Dispersiver X-ray spectroscopy (EDX) (Figure S18, Supporting Information), indicating that Bi, O, and Cl/Br are evenly distributed throughout the material, with no obvious clumping or deficiencies of elements. No other

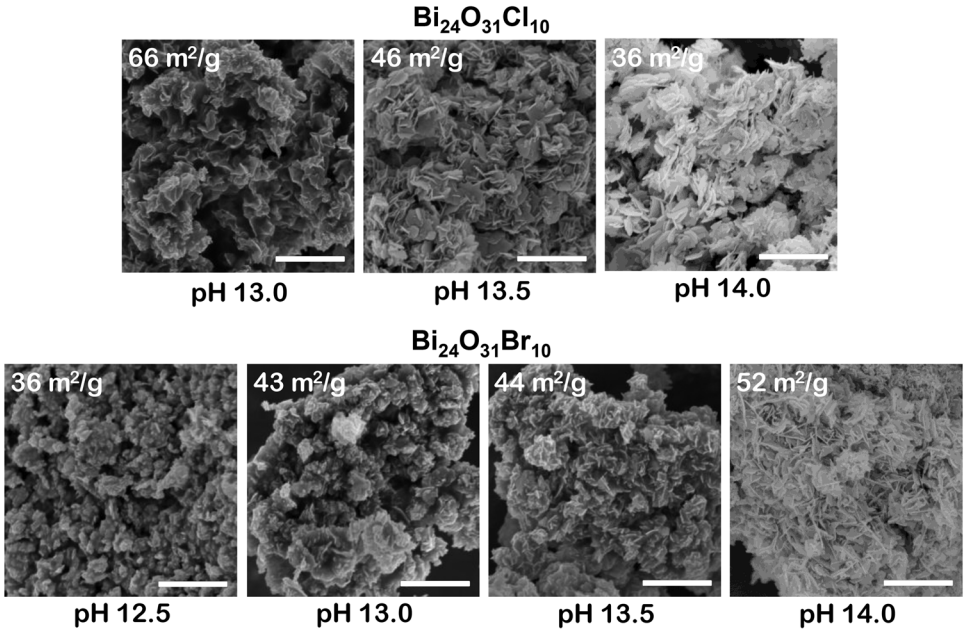

Figure 5. SEM images of $Bi_{24}O_{31}Cl_{10}$ and $Bi_{24}O_{31}Br_{10}$ powders synthesized under alkaline conditions at increasing pH. All scale bars are 1 µm. The BET surface areas of each sample are included in white in the top left corner.

significant elements were detected, indicating the purity of the materials.

The surface morphology of each of the synthesized materials was further investigated via N_2 adsorption/desorption measurements at 77 K. The Brunauer-Emett-Teller (BET)-specific surface areas determined from the data are overlaid on the SEM images in Figure 5 and also listed in Table 1. The full isotherms can be found in Figure S19 (Supporting Information). The hysteresis in all isotherms indicates that the desorption of N_2 is slow relative to adsorption. Given the dense crystal structure of $Bi_{24}O_{31}X_{10}$, a non-porous morphology is expected, and the delayed N_2 desorption is therefore suggested to arise due to the hierarchical morphology of the agglomerates. The gaps between individual nanosheets in the agglomerates likely act as mesopores, where N_2 can condense during measurements. The BET-specific surface areas increase as a function of pH for $Bi_{24}O_{31}Br_{10}$ materials and conversely decrease as a function of pH for $Bi_{24}O_{31}Cl_{10}$ materials (Table 1). As the overall agglomerate size impacts the specific surface area and the dimensions of the comprising nanosheets, correlating the surface area with the crystallite size is not trivial.

The elemental composition of the synthesized materials was assessed with XPS, and the estimated atomic compositions are included in Table 1. All HR and survey spectra are given in Figures S20–S22 (Supporting Information). The HR spectra are highly similar for all materials within a halide series, and the survey spectra reveal no discernable impurities. Extracting the approximate elemental compositions from XPS HR spectra indicates halide deficiencies in each of the synthesized materials, and the Bi:X ratio also appears to decrease as a function of pH. Although XPS is a surface-sensitive technique (probing to a depth of ≈10 nm), the ultra-thin morphology of the crystalline regions in the synthesized materials blurs the distinction between bulk and surface structure. Rather than indicating halide vacancies within the crystal structure, the indicated halide deficiencies likely relate again to the anisotropic nanosheet morphology. As the crystalline regions are ultra-thin in the stacking direction, crystallites are likely predominantly terminated along Bi–O nanosheets by the {201} and $\{10\bar{2}\}$ facets for $Bi_{24}O_{31}Cl_{10}$ and $Bi_{24}O_{31}Br_{10}$, respectively, leading to halide-deficient surfaces. The chemical composition according to Table 1 does not lead to charge-balanced compounds if Bi, O, and X attain formal oxidation states of +III, −II, and −I, respectively. Hence, XPS may not give the absolute composition, but there is a strong indication of halide deficiency. Neither quantitative STEM-EDX nor SEM-EDX analysis was performed in this study due to the beam-sensitive nature of the materials (an issue for reliable quantitative STEM-EDX) and the non-flat morphologies (an issue for quantitative SEM-EDX).

The combined analyses thus far, spanning from atomic-level structure to overall agglomerate characteristics, demonstrate a hierarchical morphology and suggest that the observed halide deficiencies are linked to the anisotropy and facet exposure of the ultra-thin nanosheets.

2.4. Trends in Photophysical Properties and Charge Carrier Dynamics, and Correlation with Structural Properties

The light absorption properties and charge carrier dynamics of the synthesized materials were investigated to correlate structural characteristics with properties relevant to photocatalytic performance. Diffuse reflectance spectroscopy (DRS) was used to examine the light absorption properties of the synthesized materials (**Figure 6**a,b), and band gaps were then estimated by producing Tauc plots from each reflectance spectrum (Figure S23, Supporting Information). All $Bi_{24}O_{31}Cl_{10}$ and $Bi_{24}O_{31}Br_{10}$

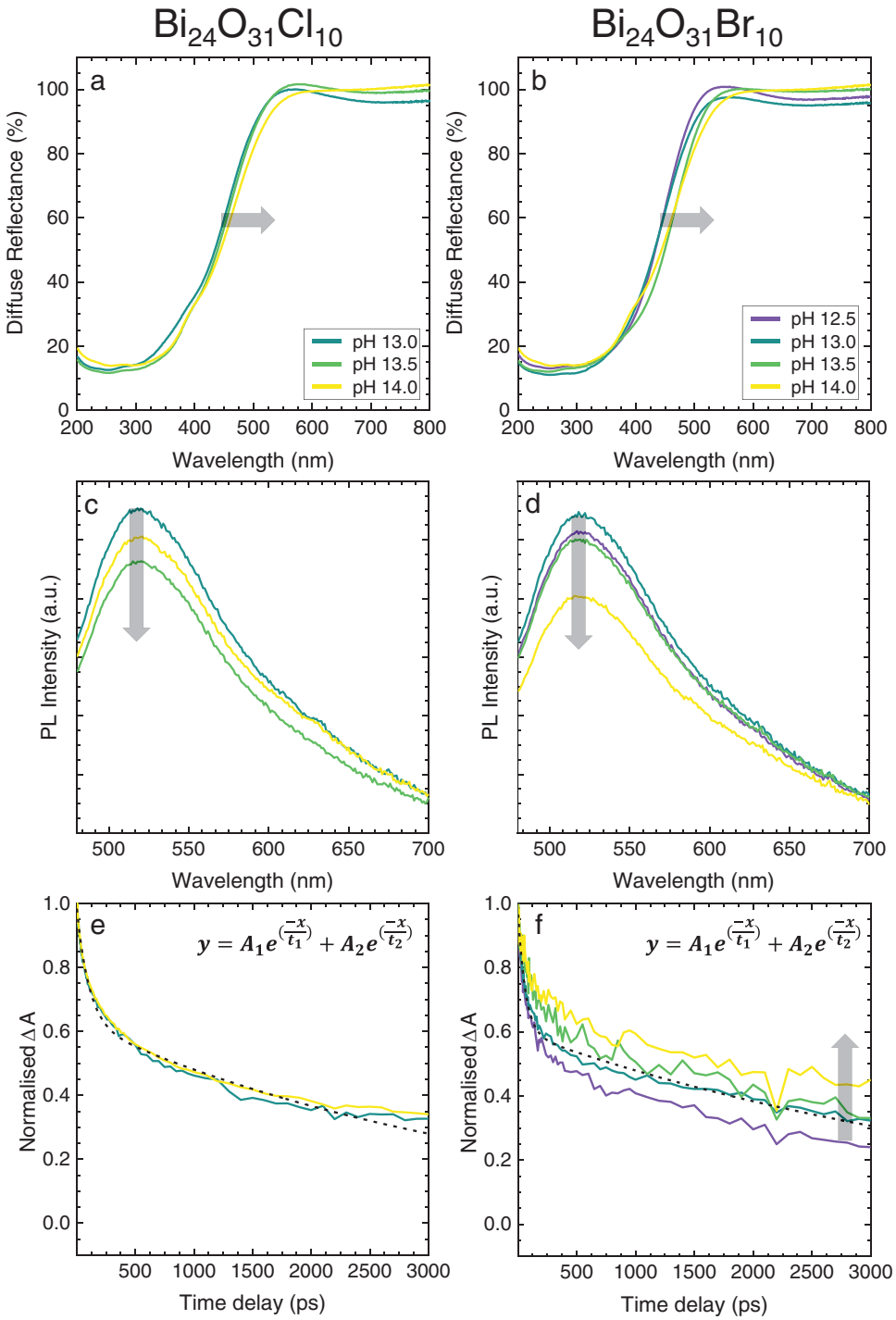

Figure 6. Reflectance spectra, PL spectra ($\lambda_{excitation}$ = 465 nm) and kinetic plots from TA spectra for a,c,e) $Bi_{24}O_{31}Cl_{10}$ and b,d,e) $Bi_{24}O_{31}Br_{10}$ powders synthesized at varied pH. Kinetic plots trace the decay in the TA signal (λ_{pump} = 400 nm) for all samples at a probe wavelength of 750 and 850 nm for the chlorides and bromides, respectively. The double exponential function used to fit the data is shown, and the fits to data for samples synthesized at pH 13.0 are included as examples with dashed black lines. Grey arrows in each plot indicate the general trend with increasing synthesis pH.

materials exhibit a sharp absorption onset, with negligible light absorption at wavelengths greater than 550 nm and increasing absorption spanning until 350 nm (Figure 6a,b). This indicates that while some visible light absorption (purple and blue light) is possible in the range of approx. 400–550 nm, absorption is strongest in the UV region, particularly for wavelengths shorter than 350 nm. The estimated band gaps were similar for all materials, spanning between 2.4 and 2.6 eV (Table 1).

Photoluminescence (PL) spectroscopy provided insight into the extent of charge recombination in each of the synthesized

Table 2. Kinetic information (amplitude and time constants) and fraction of TA signal remaining 3 ns after photoexcitation, extracted from fitting biexponential functions to the decay in TA signal for $Bi_{24}O_{31}Cl_{10}$ and $Bi_{24}O_{31}Br_{10}$ materials synthesized at varying pH.

	A_1	t_1 [ps]	A_2	t_2 [ps]	Remaining TA signal after 3 ns
$Bi_{24}O_{31}Cl_{10}$					
pH 13.0	0.36	103	0.63	3700	33%
pH 14.0	0.37	106	0.63	4140	34%
$Bi_{24}O_{31}Br_{10}$					
pH 12.5	0.41	55	0.57	3160	24%
pH 13.0	0.38	62	0.62	4480	32%
pH 13.5	0.30	114	0.65	4550	33%
pH 14.0	0.25	109	0.70	5560	45%

materials. The PL spectra in Figure 6c,d indicate that materials synthesized at lower pH generally have a larger PL signal. In contrast, the PL signal for higher pH materials is generally more "quenched". One source of PL signal in photocatalytic materials is the recombination of photogenerated electrons and holes, which limits the number of unbound charges available to participate in surface redox reactions. The trends in this study may suggest that larger crystallite sizes and lesser disorder in the higher pH materials facilitate lesser charge recombination.

A more detailed study of the generation and lifetimes of photoexcited states in the synthesized materials was conducted using femtosecond transient absorption spectroscopy (fs-TAS), with a maximum time delay after photoexcitation of 3 ns and using a visible pump (400 nm) and visible to near-IR probe spectrum (480–920 nm). All transient absorption (TA) spectra are shown in Figures S24, S25 (Supporting Information). Spectra were recorded for all samples following photoexcitation with 400 nm pump light to allow the correlation of charge carrier dynamics with the photocatalytic screenings conducted in this study using purple light.

In all spectra, the TA signal maxima occurred 1–2 ps after photoexcitation at $\lambda_{probe} \approx 750$ nm for $Bi_{24}O_{31}Cl_{10}$ materials and $\lambda_{probe} \approx 850$ nm for $Bi_{24}O_{31}Br_{10}$ materials (Figures S24–S26, Supporting Information). The signal then decays over the proceeding 3 ns, at which point a significant proportion of the TAS signal remains. This indicates that the synthesized materials facilitate charge carrier lifetimes in the order of several nanometers, which is a prerequisite for surface redox reactions to occur, given that charge transport and extraction must first proceed.[29] The proportion of TA signal remaining relative to the maxima for each spectrum is given in **Table 2**.

Normalized kinetic plots extracted from the TA spectra for each material are shown in Figure 6e,f, showing the rate of decay in the TA signal over 3 ns. A probe wavelength of 750 nm for the $Bi_{24}O_{31}Cl_{10}$ series and 850 nm for the $Bi_{24}O_{31}Br_{10}$ series was chosen to maximize the signal-to-noise ratio. The kinetic traces can be fitted with several different decay functions to give a quantitative estimation of the lifetimes of photoexcited states, and a biexponential decay function (Figure 6e,f) was found to be adequate for fitting the decay in signal from all spectra. All decay profiles and fits are shown in Figures S27–S28 (Supporting Information), and the mean lifetimes determined by fitting the data are summarized in Table 2.

For all materials, approximately one-third of the TA signal decays rapidly (A_1 in Table 2), with small time constants ranging from 55–114 ps (t_1 in Table 2). A larger proportion of the TA signal decays more slowly (A_2 in Table 2), with time constants ranging from 2750–5560 ps (t_2 in Table 2). This suggests that the decay in photoexcited states occurs through at least one fast process, such as primary germinate recombination, and at least one slower process, such as charge trapping in defect sites. No obvious trend in fitted parameters is apparent with pH for the $Bi_{24}O_{31}Cl_{10}$ series, though slightly longer excited state lifetimes are observed for the high pH sample. Within the $Bi_{24}O_{31}Br_{10}$ series, the primary and secondary time constants, t_1 and t_2, increase with pH. Additionally, the systematic increase in A_2 and decrease in A_1 throughout the series indicates that increasing proportions of the photogenerated excited states decay through slower processes. All factors indicate longer excited state lifetimes in higher pH materials.

Although pinpointing the precise causal relationship between structural characteristics and charge carrier dynamics is beyond the scope of the present study, our results already indicate that tuning the synthesis pH for $Bi_{24}O_{31}X_{10}$ materials impacts the photophysical properties and charge carrier dynamics. Increased synthesis pH correlates with slower TA signal decay, suggesting that larger crystalline domains and lesser disorder may facilitate longer excited state lifetimes. Only limited comparisons can be made with existing literature, as to the best of our knowledge, no equivalent studies provide insight into correlating detailed structural analyses with charge carrier dynamics for such complex, polycrystalline photocatalytic materials. However, one recent study focusing on commercial TiO_2 photocatalysts found that larger particle size was correlated with longer excited state lifetimes, which was explained by the lower proportion of surface charge trapping sites in larger particles.[30] A similar phenomenon may explain the comparatively long lifetimes in larger crystallites in the present study, with fewer defects and lesser disordered content in the higher pH materials, minimizing charge recombination and/or trapping.

2.5. Trends in Photocatalytic Properties and Discussion of the Structure-Property-Performance Relationship

The pH-induced trends in photocatalytic properties were investigated by considering the photo-oxidation of benzylamine to N-benzylidenebenzylamine (**Scheme 1**) under visible light illumination (410 nm). This model reaction was selected due to the documented ability of bismuth oxyhalides to facilitate similar organic oxidation/reduction reactions.[3b] However, as the focus of this study was not on achieving complete or rapid conversion, as has already been reported elsewhere,[3c,31] experimental conditions were tailored to document trends in photocatalytic performance.

Figure 7a,b shows the yields of N-benzylidenebenzylamine produced after 24 h of constant illumination for $Bi_{24}O_{31}Cl_{10}$ and $Bi_{24}O_{31}Br_{10}$, respectively, demonstrating that all synthesized materials perform as photocatalysts under violet light

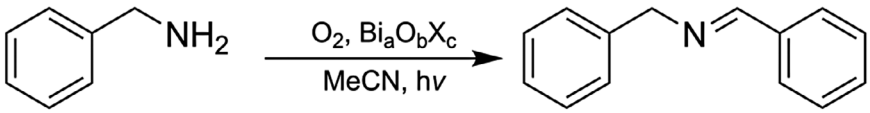

Scheme 1. Reaction scheme for the oxidation of benzylamine to N-benzylidenebenzylamine in acetonitrile (MeCN) in the presence of oxygen, incident light, and a bismuth oxyhalide photocatalyst.

illumination (data is included in Table S12, Supporting Information). Blank screenings were also conducted, involving the omission of light or photocatalyst, achieving negligible conversion (Table S13, Supporting Information). The photocatalytic performance of the $Bi_{24}O_{31}Br_{10}$ materials synthesized at pH 12.5 and pH 13.0 is very similar, as is the performance for materials synthesized at pH 13.5 and 14.0 within each halide series, corresponding well with the generally similar properties of these pairs of materials throughout the study. For the $Bi_{24}O_{31}Cl_{10}$ materials, the performance recedes with pH, while the performance improves with pH for the $Bi_{24}O_{31}Br_{10}$ materials.

Figure 7c shows that the performance of the materials remains relatively constant with repeated use (data is included in Table S14, Supporting Information), while Figure 7d shows that the crystal structure of the photocatalyst is unchanged after conducting photocatalytic screenings. Thus, the Bi-rich bismuth oxyhalides show promising trends concerning stability under visible light illumination, repeated use, and chemical exposure.

Given the many interrelated factors impacting any photocatalytic system, isolating a single parameter that facilitates improved photocatalytic properties is not trivial. However, the trends in photocatalytic properties in this study are closely correlated with the BET surface areas of the materials, suggesting that increased surface area is the primary factor contributing to improved photocatalytic properties. For the $Bi_{24}O_{31}Br_{10}$ series, the trends in photocatalytic performance also correlate

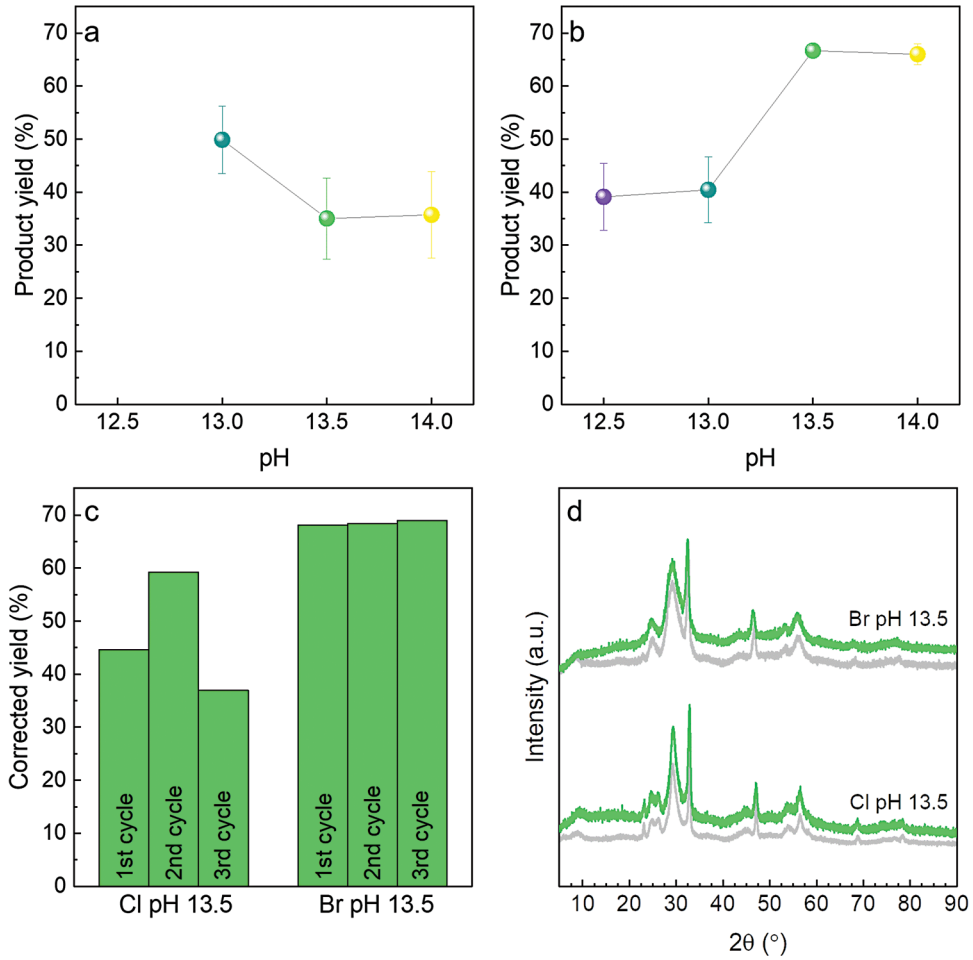

Figure 7. Trends in photocatalytic activity of a) $Bi_{24}O_{31}Cl_{10}$ and b) $Bi_{24}O_{31}Br_{10}$ photocatalysts synthesized at varying pH values, when irradiated with 410 nm light. Purple, teal, green, and yellow markers indicate data for materials synthesized at pH 12.5, 13.0, 13.5, and 14.0, respectively. All tests are based on 24 h irradiation, and each data point is based on at least three independent tests. c) shows product yields during recycling tests for $Bi_{24}O_{31}Cl_{10}$ and $Bi_{24}O_{31}Br_{10}$ synthesized at pH 13.5 and d) shows PXRD patterns before use (grey line) and after use (green line).

with the photophysical properties, suggesting that extended excited state lifetimes facilitated by larger crystalline domains also contribute to improved photocatalytic performance. The increased surface area likely contributes to more accessible catalytic active sites for redox reactions to proceed. At the same time, the longer lifetimes of photoexcited states, facilitated by larger crystallites and lesser disorder, likely lead to greater availability of free charge carriers to participate in surface redox reactions.

The combined results of this study suggest that an ideal $Bi_{24}O_{31}X_{10}$ photocatalyst should consist of large crystalline domains with few defects and little disorder whilst also maintaining small particle sizes and, therefore, large surface areas. Developing small, monocrystalline particles of $Bi_{24}O_{31}X_{10}$ would satisfy all of these factors and could, therefore, facilitate optimal photocatalytic properties.

3. Conclusion

A series of Bi-rich bismuth oxyhalides were synthesized under alkaline conditions (pH > 12.5), by performing a precipitation reaction followed by a microwave heating step. The high level of disorder, small crystalline regions, and a large number of structurally similar Bi-rich compounds contribute to the historical difficulties in allocating the crystal phase of such materials. However, incorporating 4D-STEM and synchrotron PXRD analyses in this study reveals the crystal phase to be $Bi_{24}O_{31}X_{10}$ (X = Cl, Br). The crystalline domains are highly anisotropic, retaining long-range order in in-plane directions but lacking order in the stacking direction of the layers. The anisotropic platelets comprised ≈7–10 layers bound together. These platelets agglomerate together to form micron-sized flower-like polycrystalline particles. As a result, the overall BET-specific surface area does not necessarily reflect the size of the individual crystalline domains.

Further structural investigations with X-ray- and neutron PDF analyses indicate that increasing the synthesis pH facilitates the formation of larger and more ordered crystalline regions. The larger crystalline domains of the samples synthesized at higher pH correlate with longer excited state lifetimes, according to fs-TAS analyses. This may have contributed toward improving the photocatalytic properties (using the photo-oxidation of benzylamine as a model reaction). However, the most dominant factor that influenced the photocatalytic properties was increased surface area.

Our detailed structure-property study has enabled the phase allocation of a complex, polycrystalline photocatalyst, which is widely debated in the literature. Furthermore, we have provided a much-needed and detailed discussion of the link between structural properties (including the size and anisotropy of crystalline domains and level of disorder) and photocatalytic properties (including facet exposure, surface area, and excited state lifetimes) to inform future studies.

4. Experimental Section

Synthesis: All chemicals were purchased from Merck and used as supplied without further purification. $Bi_{24}O_{31}Cl_{10}$ and $Bi_{24}O_{31}Br_{10}$ were synthesized using a procedure adapted from Marks et al.,[1] where NaCl (0.27 g, 4.5 mmol) or NaBr (0.46 g, 4.5 mmol), respectively, were added to a conical flask along with $Bi(NO_3)_3.5H_2O$ (0.14 g, 0.30 mmol), deionized water (8.7 mL) and HNO_3 (1.3 mL, 65%). After stirring for 10 min, an aqueous solution of KOH (4 $_M$) was added dropwise to adjust the pH of the suspension while stirring in an ice bath. After stirring for an additional 30 min, the suspension containing the white precursor powder was heated in a food-grade microwave (Logik L17MW14E) for 4 min (200 W). After cooling the suspension, the yellow precipitate was collected by filtration, rinsed with water and ethanol, and dried in an oven (60 °C, 12 h). Yields of 50–70 mg (70–95%) were typically obtained, and multiple batches were typically mixed before characterization or photocatalytic screening. This was intended to prevent any small batch-to-batch variations from impacting the results.

Characterization: Synchrotron Powder X-ray Diffraction (PXRD): HR synchrotron PXRD data was collected in transmission (Debye-Scherer geometry) at beamline P02.1, PETRA III, at the Deutsches Elektronen-Synchrotron (DESY) in Hamburg, Germany. Powder samples were packed into Kapton capillaries (1.0 mm diameter), and measurements were then conducted using an X-ray wavelength of 0.2073 Å, and a sample-to-detector distance of 140.2 cm (calibrated using a NIST LaB_6 SRM660A standard). The Varex detector was positioned centered behind the sample capillary, allowing the collection of full Debye-Scherer rings over a 2θ range of 0.188–22.8°. Three measurements were taken for each sample over a total of 3 min, and the diffractograms were summed using pyFAi.[2] Any necessary masking was applied in the same software to remove contributions from the beam stop and any dead pixels in the detector before integrating the summed 2D diffractograms to produce 1D diffraction patterns. Experimental diffraction patterns were compared with calculated patterns produced in VESTA,[3] using CIF data for $Bi_aO_bX_c$ phases found in the ICSD.

Characterization: Laboratory Powder X-ray Diffraction (PXRD): Laboratory PXRD data was collected using a Panalytical Aeris benchtop diffractometer equipped with a PIXcel1D detector in Bragg-Brentano geometry, using Cu $K_{\alpha1}$ (1.54056 Å) and $K_{\alpha2}$ (1.54439 Å) radiation. Measurements were recorded over 40 min using a flat, low-background silicon sample holder.

Characterization: Scanning Transmission Electron Microscopy and Energy Dispersive X-ray Spectroscopy (STEM-EDX): The powdered samples were suspended in ethanol (99.9%) and subsequently drop-casted onto Cu 300 mesh Lacey carbon grids coated with ultra-thin carbon (≈2 nm) (Plano GmbH). STEM images were collected using a Talos FX-200 microscope operating at 200 keV. A convergence angle of 10.5 mrad was used, and the collection angle of the STEM high-angle annular dark-field (HAADF) images was 60–200 mrad. STEM-EDX datasets were collected using the ChemiSTEM system installed on the Talos microscope. Data analysis and plotting were performed using HyperSpy,[4] SciPy,[5] NumPy,[6] and Scikit-image.[7] Due to the highly beam-sensitive nature of the samples, EDX data collection was performed at low beam currents, relatively low magnification, and only for a long enough duration to verify the spatial homogeneity elemental distribution without achieving good enough counting statistics for proper quantitative EDX analysis.

Characterization: Four Dimensional Scanning Electron Microscopy (4D-STEM): 4D-STEM data were collected on the same microscope on a MerlinEM 4R Quad chip 512 × 512 detectors (Quantum detectors). A 20 µm C2 condenser aperture was used in nanoprobe mode, which resulted in a convergence angle of 3.0 mrad and an approx. footprint of the beam of 1.5 nm. An exposure time of 0.008s pr pixel was used and the data was collected in (2x) 12-bit mode. With the low dose conditions used, these parameters provided the optimal balance between data quality and avoiding beam damage. The scanning electron nanobeam diffraction (SEND) patterns were collected over sample areas of 128 × 128 pixels with a probe step size matching the approx. footprint of the beam (1.5 nm). vADF images were prepared using the open-source software LiberTEM.[8] PASEND patterns were prepared from selected regions of interest (ROI) using LiberTEM. Individual position average SEND patterns were indexed using the software Single Crystal.[9]

Characterization: X-ray Total Scattering (TS) and Pair Distribution Function (PDF) Analysis: X-ray total scattering (TS) data was collected at beamline P02.1, PETRA III, at the Deutsches Elektronen-Synchrotron

(DESY) in Hamburg, Germany, and used for X-ray PDF analysis. Powder samples were packed into Kapton capillaries (1.0 mm diameter), and fifteen 2D scattering images of each sample were collected over a total of 15 min at 59.80 keV (0.2073 Å). The 2D detector was arranged behind the sample to collect quarter Debye-Scherrer rings to maximize Q resolution. A sample-to-detector distance of 30.14 cm was calibrated using a LaB_6 standard sample (NIST LaB_6 SRM660a), resulting in a Q_{max} of 22 $Å^{-1}$. However, a slightly smaller Q_{max} was used to exclude noisy data in the high Q region for some samples. The fifteen 2D diffractograms for each sample were summed and integrated using pyFAi,[2] and the *x*PDF*suite* software[10] was used to obtain PDFs, $G(r)$, by applying a Fourier transform to the integrated data, after background subtraction of the diffracted intensity of an empty Kapton capillary. Refinement of a LaB_6 standard in PDF*gui*[11] allowed the determination of $Q_{damp} = 0.02838$ Å, and $Q_{broad} = 0.002534$ Å, which represent the instrumental contributions to PDF dampening and broadening. Theoretical PDFs were calculated with PDF*gui*, using CIF data from the ICSD. Experimental PDFs were also refined using PDF*gui*. The scale factor, unit cell parameters (a, b, c, β), and low-symmetry Bi atomic positions (x, z) were refined over the r-range of 1–15 Å.

Characterization: Neutron Total Scattering (TS) and Pair Distribution Function (PDF) Analysis: Neutron TS data was collected at the Nanoscale Ordered Materials Diffractometer (NOMAD) at the Spallation Neutron Source (SNS, Oak Ridge National Laboratory). ≈60 mg of each powder sample was loaded into sealed quartz tubes, and measurements were conducted at 300 K. Experimental PDFs were calculated by beamline staff.

Characterization: Scanning Electron Microscopy (SEM): SEM images were collected using an FEI-Nova SEM 600 scanning electron microscope at 50 000x magnification. SEM samples were produced by thinly dispersing each powder sample onto carbon tape and coating them with a 7.0 nm layer of platinum using a LEICA EM SCD 500 vacuum film deposition system.

Characterization: N_2 Adsorption/Desorption: Nitrogen adsorption and desorption measurements were performed using a Micrometrics TriStar II 3020 instrument at 77 K, after first outgassing the samples under inert gas flow for 16 h at 80 °C, using a Micrometrics SmartPrep Programmable Degas System. ≈ 100 mg of each sample was used in the measurements, and BET surface areas were estimated using Micrometrics commercial software by considering the straight line fitted through the data points in the P/P_0 range of 0.05–0.3.

Characterization: X-ray Photoelectron Spectroscopy (XPS): XPS measurements were performed under high vacuum using an Axis Ultra DLD instrument (Kratos Analytical) at 225 W and using a monochromated Al Kα radiation source. HR and survey spectra were recorded using pass energies of 20 and 160 eV, respectively, with an estimated penetration depth of ≈ 10 nm. All spectra were processed using CasaXPS,[12] and the carbon 1s peak at 284.8 eV was used for calibration. Carbon 1s and oxygen 1s peaks were fitted using a GL(30) or GL(50) function and Shirley backgrounds. The atomic surface concentrations represent the average of survey scans taken at three different spots on each sample.

Characterization: Diffuse Reflection (DRS) Spectroscopy: Absorbance and DRS data were collected using a PerkinElmer Lambda 1050S UV/VIS/NIR spectrophotometer equipped with an integrating sphere and using $BaSO_4$ powder as a white background material. Absorbance and reflectance data were collected in the UV-visible wavelength range of 200–800 nm. After applying the Kubelka-Munk function to the reflectance data, the band gap (E_g) of each material was estimated by producing Tauc plots.

Characterization: Photoluminescence (PL) Spectroscopy: PL spectroscopy measurements were conducted using an Edinburgh instrument FLS980 instrument equipped with an integrating sphere and $BaSO_4$ as a white reference standard. Emission scans were conducted with an excitation wavelength of 465 nm, over the 480–700 nm emission range.

Characterization: Femtosecond Transient Absorption Spectroscopy (fs-TAS): fs-TAS was performed using a visible pump laser (400 nm) and a visible probe spectrum (500–900 nm). During measurements, samples were excited by 180 fs laser pulses generated using a YKGBW oscillator (Light Conversion, Pharos SP) at λ = 1028 nm through nonlinear frequency mixing in an optical parametric amplifier (OPA) and second harmonics module (Light Conversion, Orpheus). A small fraction of the fundamental beam was split to generate the broadband probe spectrum in a sapphire crystal (500–1600 nm). The probe pulse was delayed relative to the pump pulse using a delay stage, with a maximum delay of 3 ns. The pump and probe pulses overlap on the sample position at an angle of ≈ 8 °, after which the probe light is led to a detector (Ultrafast Systems, Helios). The pump laser intensity ranged between 5.3-5.6 mW.cm^{-2}.

Powder samples were prepared for measurements by adding 50 mg of powder to an Eppendorf tube with 14 mL of MilliQ water and sonicated for 30 min to disperse the powder. Based on Stoke's law of sedimentation, the sample tubes were left to settle for approximately one hour to allow the largest particles to settle to the bottom of the tubes. The smallest particles remaining at the top of the suspension were added to a 2 mm quartz cuvette, as the smaller particles had a lesser scattering effect and greater dispersion stability in water.

Photocatalytic Screenings: In a typical photocatalytic screening, the photocatalyst (25 mg) was added to the reaction chamber (122 mL total volume) along with benzylamine (11 mg, 1 mmol, 109 µL), and dispersed in acetonitrile (10 mL). The reaction chamber was mostly sealed during the reaction, except for a valve that remained open to atmospheric oxygen. After stirring in the dark for 10 min to equilibrate the system, the suspensions were irradiated with LED light (410 nm, Spectroline) whilst stirring for 24 h. After the reaction, the catalyst was separated via centrifugation, and the solvent was removed under reduced pressure, leaving only the liquid reactant and product mixture. The quantity of the yellow product was determined using ^{1}H NMR spectroscopy (Bruker Ascend, 400 MHz) in $CDCl_3$, after adding mesitylene (13 mg, 0.11 mmol, 15 µL) as an internal standard. Each photocatalytic screening was repeated at least three times to ensure reproducibility. To perform recycling tests and post-mortem characterization of the materials, selected catalysts were separated via centrifugation, rinsed with ethanol, dried, and stored for future use.

The authors have cited additional references within the Supporting Information.[7c,12,16,32]

Supporting Information

Supporting Information is available from the Wiley Online Library or from the author.

Acknowledgements

The work was supported by the Independent Research Fund Denmark (8021-00349B), the Center for Integrated Materials Research (iMAT) at Aarhus University, the Carlsberg Foundation (CF17-0937 and CF18-0840), the Danish National Research Foundation (Carbon Dioxide Activation Center, DNRF 118), and Danscatt. MAvdV and JK are grateful for funding from the Dutch research council (NWO) (project number VI.Vidi 193.151) via the NWO Talent Program VIDI. The authors acknowledge DESY (Hamburg, Germany), a member of the Helmholtz Association HGF, for the provision of experimental facilities. Parts of this research were carried out at beamline P02.1, PETRA III. Beamtime at P02.1 was allocated by an In-House contingent. A portion of this research used resources at the Spallation Neutron Source, a DOE Office of Science User Facility operated by the Oak Ridge National Laboratory (proposal 28835.1). Beamline staff at NOMAD are kindly acknowledged for data collection and reduction.

Conflict of Interest

The authors declare no conflict of interest.

Data Availability Statement

The data that support the findings of this study are available from the corresponding author upon reasonable request.

Keywords

disordered functional materials, layered materials, structure-activity relationships, time-resolved spectroscopy

Received: March 25, 2024
Revised: April 25, 2024
Published online: May 11, 2024

[1] a) Z. Kuspanov, B. Bakbolat, A. Baimenov, A. Issadykov, M. Yeleuov, C. Daulbayev, *Sci. Total Environ.* **2023**, *885*, 163914; b) Y. J. Xu, *Front. Catal.* **2021**, *1*, 708319.

[2] a) Q. C. Liu, D. K. Ma, Y. Y. Hu, Y. W. Zeng, S. M. Huang, *ACS Appl. Mater. Interfaces* **2013**, *5*, 11927; b) K. Kouvelis, A. A. Ioannidi, A. Petala, M. Souliotis, Z. Frontistis, *Catalysts* **2023**, *13*, 1175; c) C. Y. Wang, X. Zhang, H. B. Qiu, G. X. Huang, H. Q. Yu, *Appl. Catal., B* **2017**, *205*, 615; d) Z. Wang, Z. Chu, C. Dong, Z. Wang, S. Yao, H. Gao, Z. Liu, Y. Liu, B. Yang, H. Zhang, *ACS Appl. Nano Mater.* **2020**, *3*, 1981.

[3] a) Y. Dai, C. Li, Y. Shen, S. Zhu, M. S. Hvid, L. C. Wu, J. Skibsted, Y. Li, J. W. H. Niemantsverdriet, F. Besenbacher, N. Lock, R. Su, *J. Am. Chem. Soc.* **2018**, *140*, 16711; b) Y. Dai, P. Ren, Y. Li, D. Lv, Y. Shen, Y. Li, H. Niemantsverdriet, F. Besenbacher, H. Xiang, W. Hao, N. Lock, X. Wen, J. P. Lewis, R. Su, *Angew. Chem., Int. Ed.* **2019**, *58*, 6265; c) A. Han, H. Zhang, G. K. Chuah, S. Jaenicke, *Appl. Catal., B* **2017**, *219*, 269.

[4] a) Y. Bai, P. Yang, L. Wang, B. Yang, H. Xie, Y. Zhou, L. Ye, *Chem. Eng. J.* **2019**, *360*, 473; b) J. Di, P. Song, C. Zhu, C. Chen, J. Xiong, M. Duan, R. Long, W. Zhou, M. Xu, L. Kang, B. Lin, D. Liu, S. Chen, C. Liu, H. Li, Y. Zhao, S. Li, Q. Yan, L. Song, Z. Liu, *ACS Mater. Lett.* **2020**, *2*, 1025; c) J. Di, C. Zhu, M. Ji, M. Duan, R. Long, C. Yan, K. Gu, J. Xiong, Y. She, J. Xia, H. Li, Z. Liu, *Angew. Chem., Int. Ed.* **2018**, *57*, 14847.

[5] a) G. J. Lee, Y. C. Zheng, J. J. Wu, *Catal. Today* **2018**, *307*, 197; b) L. Zhang, W. Wang, S. Sun, D. Jiang, E. Gao, *Appl. Catal., B* **2015**, *162*, 470.

[6] S. Wang, X. Hai, X. Ding, K. Chang, Y. Xiang, X. Meng, Z. Yang, H. Chen, J. Ye, *Adv. Mater.* **2017**, *29*, 1701774.

[7] a) C. Bi, J. Cao, H. Lin, Y. Wang, S. Chen, *RSC Adv.* **2016**, *6*, 15525; b) H. L. Chen, W. W. Lee, W. H. Chung, H. P. Lin, Y. J. Chen, Y. R. Jiang, W. Y. Lin, C. C. Chen, *J. Taiwan Inst. Chem. Eng.* **2014**, *45*, 1892; c) M. Marks, H. S. Jeppesen, N. Lock, *ACS Appl. Mater. Interfaces* **2022**, *14*, 23496.

[8] J. Di, J. Xia, H. Li, S. Guo, S. Dai, *Nano Energy* **2017**, *41*, 172.

[9] K. G. Keramidas, G. P. Voutsas, P. I. Rentzeperis, Z. Kristallogr, *Cryst. Mater.* **1993**, *205*, 35.

[10] H. Kodama, S. Horiuchi, A. Watanabe, *J. Solid State Chem.* **1988**, *75*, 279.

[11] F. Hopfgarten, *Acta Crystallogr., Sect. B: Struct. Sci., Cryst. Eng. Mater.* **1976**, *32*, 2570.

[12] A. Aliev, J. Olchowka, M. Colmont, E. Capoen, C. Wickleder, O. Mentré, *Inorg. Chem.* **2013**, *52*, 8427.

[13] J. Ketterer, V. Kramer, *Acta Crystallogr., Sect. C: Struct. Chem.* **1986**, *42*, 1098.

[14] B. Aurivillius, *Chem. Scr.* **1984**, *24*, 125.

[15] E. Keller, V. Krämer, M. Schmidt, H. Oppermann, Z. Kristallogr, *Cryst. Mater.* **2002**, *217*, 256.

[16] U. Eggenweiler, E. Keller, V. Kramer, *Acta Crystallogr., Sect. B: Struct. Sci., Cryst. Eng. Mater.* **2000**, *56*, 431.

[17] E. Keller, V. Krämer, *Acta Crystallogr., Sect. C: Struct. Chem.* **2007**, *63*, i109.

[18] a) X. Jin, L. Ye, H. Xie, G. Chen, *Coord. Chem. Rev.* **2017**, *349*, 84; b) X. Xiao, C. Liu, R. Hu, X. Zuo, J. Nan, L. Li, L. Wang, *J. Mater. Chem.* **2012**, *22*, 22840.

[19] L. G. Sillén, M. Edstrand, Z. Kristallogr, *Cryst. Mater.* **1942**, *104*, 178.

[20] a) J. Jiang, K. Zhao, X. Xiao, L. Zhang, *J. Am. Chem. Soc.* **2012**, *134*, 4473; b) L. Wang, J. Shang, W. Hao, S. Jiang, S. Huang, T. Wang, Z. Sun, Y. Du, S. Dou, T. Xie, D. Wang, J. Wang, *Sci. Rep.* **2014**, *4*, 7384.

[21] a) J. Li, L. Zhang, Y. Li, Y. Yu, *Nanoscale* **2014**, *6*, 167; b) H. Zhang, Y. Yang, Z. Zhou, Y. Zhao, L. Liu, *J. Phys. Chem. C* **2014**, *118*, 14662.

[22] a) S. Vinoth, W. J. Ong, A. Pandikumar, *Coord. Chem. Rev.* **2022**, *464*, 214541; b) L. Zhang, W. Wang, D. Jiang, E. Gao, S. Sun, *Nano Res.* **2015**, *8*, 821; c) X. Y. Kong, W. P. C. Lee, W. J. Ong, S. P. Chai, A. R. Mohamed, *ChemCatChem* **2016**, *8*, 3074; d) X. Xiao, C. Zheng, M. Lu, L. Zhang, F. Liu, X. Zuo, J. Nan, *Appl. Catal., B* **2018**, *228*, 142; e) J. Wu, X. Li, W. Shi, P. Ling, Y. Sun, X. Jiao, S. Gao, L. Liang, J. Xu, W. Yan, C. Wang, Y. Xie, *Angew. Chem., Int. Ed.* **2018**, *57*, 8719.

[23] a) J. Han, G. Zhu, M. Hojamberdiev, J. Peng, P. Liu, *Mater. Lett.* **2016**, *169*, 122; b) S. Fu, G. Li, X. Wen, C. Fan, J. Liu, X. Zhang, R. Li, *Trans. Nonferrous Met. Soc. China* **2020**, *30*, 765.

[24] L. Ye, X. Jin, C. Liu, C. Ding, H. Xie, K. H. Chu, P. K. Wong, *Appl. Catal., B* **2016**, *187*, 281.

[25] J. Shang, W. Hao, X. Lv, T. Wang, X. Wang, Y. Du, S. Dou, T. Xie, D. Wang, J. Wang, *ACS Catal.* **2014**, *4*, 954.

[26] a) X. Jin, C. Lv, X. Zhou, H. Xie, S. Sun, Y. Liu, Q. Meng, G. Chen, *Nano Energy* **2019**, *64*, 103955; b) X. Jin, C. Lv, X. Zhou, L. Ye, H. Xie, Y. Liu, H. Su, B. Zhang, G. Chen, *ChemSusChem* **2019**, *12*, 2740.

[27] M. Guan, C. Xiao, J. Zhang, S. Fan, R. An, Q. Cheng, J. Xie, M. Zhou, B. Ye, Y. Xie, *J. Am. Chem. Soc.* **2013**, *135*, 10411.

[28] J. Li, Y. Yu, L. Zhang, *Nanoscale* **2014**, *6*, 8473.

[29] T. J. Miao, J. Tang, *J. Chem. Phys.* **2020**, *152*, 194201.

[30] S. Nakajima, R. Katoh, *J. Mater. Chem. A* **2015**, *3*, 15466.

[31] W. Zhao, C. Yang, X. Zhang, Y. Deng, C. Han, Z. Ma, L. Wang, L. Ye, *ChemSusChem* **2020**, *13*, 116.

[32] a) J. Kieffer, V. Valls, N. Blanc, C. Hennig, *J. Synchrotron Radiat.* **2020**, *27*, 558; b) K. Momma, F. Izumi, *J. Appl. Crystallogr.* **2011**, *44*, 1272; c) T. Aarholt, P. Burdet, G. Donval, A. Eljarrat, T. Furnival, A. Garmannslund, I. Iyengar, C. Jan, D. N. Johnstone, P. Jokubauskas, K. E. MacArthur, B. Martineau, S. Mazzucco, V. Migunov, M. Nord, T. Ostasevicius, E. Prestat, M. Sarahan, J. Taillon, V. Tonaas Fauske, M. Walls, F. Winkler, L.-F. Zagonel, F. de la Pena, *Microsc. Microanal.* **2017**, *23*, 214; d) P. Virtanen, R. Gommers, T. E. Oliphant, M. Haberland, T. Reddy, D. Cournapeau, E. Burovski, P. Peterson, W. Weckesser, J. Bright, S. J. van der Walt, M. Brett, J. Wilson, K. J. Millman, N. Mayorov, A. R. J. Nelson, E. Jones, R. Kern, E. Larson, C. J. Carey, İ. Polat, Y. Feng, E. W. Moore, J. VanderPlas, D. Laxalde, J. Perktold, R. Cimrman, I. Henriksen, E. A. Quintero, C. R. Harris, et al., *Nat. Methods* **2020**, *17*, 261; e) C. R. Harris, K. J. Millman, S. J. van der Walt, R. Gommers, P. Virtanen, D. Cournapeau, E. Wieser, J. Taylor, S. Berg, N. J. Smith, R. Kern, M. Picus, S. Hoyer, M. H. van Kerkwijk, M. Brett, A. Haldane, J. F. del Río, M. Wiebe, P. Peterson, P. Gérard-Marchant, K. Sheppard, T. Reddy, W. Weckesser, H. Abbasi, C. Gohlke, T. E. Oliphant, *Nature* **2020**, *585*, 357; f) S. Van der Walt, J. L. Schönberger, J. Nunez-Iglesias, F. Boulogne, J. D. Warner, N. Yager, E. Gouillart, T. Yu, *PeerJ* **2014**, *2*, 453; g) A. Clausen, D. Weber, K. Ruzaeva, V. Migunov, A. Baburajan, A. Bahuleyan, J. Caron, R. Chandra, S. Halder, M. Nord, *J. Open Source Softw.* **2020**, *5*, 2006. h) D. C. Palmer, Z. Kristallogr, *Cryst. Mater.* **2015**, *230*, 559; i) X. Yang, P. Juhas, C. Farrow, S. Billinge, arXiv **2014**, 1402.3161v3; j) C. L. Farrow, P. Juhas, J. W. Liu, D. Bryndin, E. S. Božin, J. Bloch, T. Proffen, S. J. L. Billinge, *J. Phys.: Condens. Matter* **2007**, *19*, 335219; k) N. Fairley, V. Fernandez, M. Richard-Plouet, C. Guillot-Deudon, J. Walton, E. Smith, D. Flahaut, M. Greiner, M. Biesinger, S. Tougaard, D. Morgan, J. Baltrusaitis, *Appl. Surf. Sci. Adv.* **2021**, *5*, 100112; l) D. Prieur, W. Bonani, K. Popa, O. Walter, K. W. Kriegsman, M. H. Engelhard, X. Guo, R. Eloirdi, T. Gouder, A. Beck, T. Vitova, A. C. Scheinost, K. Kvashnina, P. Martin, *Inorg. Chem.* **2020**, *59*, 5760.